

# Perceiving and Reasoning About Liquids Using Fully Convolutional Networks

Connor Schenck<sup>1</sup> and Dieter Fox<sup>1</sup>

The International Journal of Robotics Research  
 XX(X):1–22  
 ©The Author(s) 2017  
 Reprints and permission:  
[sagepub.co.uk/journalsPermissions.nav](http://sagepub.co.uk/journalsPermissions.nav)  
 DOI: 10.1177/ToBeAssigned  
[www.sagepub.com/](http://www.sagepub.com/)



## Abstract

Liquids are an important part of many common manipulation tasks in human environments. If we wish to have robots that can accomplish these types of tasks, they must be able to interact with liquids in an intelligent manner. In this paper, we investigate ways for robots to perceive and reason about liquids. That is, the robots ask the questions *What in my sensory data stream is liquid?* and *How can I use that to infer all the potential places liquid might be?* We collected two datasets to evaluate these questions, one using a realistic liquid simulator and another on our robot. We used fully convolutional neural networks to learn to detect and track liquids across pouring sequences. Our results show that our networks are able to perceive and reason about liquids, and that integrating temporal information is important to performing these tasks well.

## Keywords

Detection & Tracking, Image Segmentation, Liquid Learning

## Introduction

Liquids are ubiquitous in human environments. Humans perform many of their daily actions using liquids, whether it is pouring coffee, mixing ingredients for a recipe, or washing their hands. Any general purpose robot that will operate in a human environment must thus be able to robustly handle liquids. This is a difficult challenge though. Unlike rigid objects, liquids follow complicated dynamics and aren't necessarily divisible into well-defined objects.

### Acknowledgments:

We would like to acknowledge the assistance of Sudharsan Prabu in helping collect data for this paper.

<sup>1</sup>University of Washington, Seattle, WA, USA

### Corresponding author:

Connor Schenck

Email: schenckc@cs.washington.edu

But before a robot can even begin to manipulate liquids, it first must be able to perceive and reason about them. For example, solving tasks such as pouring requires both robust control *and* detection of liquid during the pouring operation. Thus controlling liquids requires close closed-loop sensory feedback to perform well. This is a difficult problem in itself. For example, many liquids are transparent, making them hard to see in a color image. Additionally, modern approaches to finding rigid objects in a scene often rely on using a depth sensor, which do not apply to liquids as many of them are not visible on depth sensors. In this paper, we investigate ways to solve this task.

Specifically, we examine the problems of *perceiving* and *reasoning* about liquids. That is, we ask the questions *What in the raw visual data stream is liquid?* and *Can that be used to infer all places where liquid might be?* To solve these problems, we take advantage of recent advances in the field of

deep learning. This approach has been extremely successful in various areas of computer vision, including classification (Krizhevsky et al., 2012), semantic labeling (Farabet et al., 2013), and pose regression (Girshick et al., 2011), and it enabled computers to successfully play Atari games from raw image data (Guo et al., 2014) and train end-to-end policies on robots (Levine et al., 2015). The ability of deep networks to process and make sense of raw sensory data, especially raw visual data, makes them a good fit for perceiving and reasoning about liquids from raw visual data.

In this paper, we focus on the task of pouring as our exemplar task for learning about liquids. We utilize fully-convolutional networks (FCNs), networks without any fully-connected layers, to solve the problems of *perception* and *reasoning* about liquids. We generate a large dataset in a realistic liquid simulator for evaluating our networks. We also collect a dataset of pouring trials on a real robot using a thermal camera to get the ground truth. Additionally, we evaluate different types of input images to test the generalization ability of our methodology.

Our results show that the methodology we propose in this paper is able to both *perceive* and *reason* about liquids. Specifically, they show that our recurrent networks are well-suited to these tasks, as they are able to integrate information over time in a useful manner. We also show that, with the right type of input image, our neural networks can generalize to new data with objects that are not included in the training set. These results strongly suggest that our deep learning approach to these problems is useful in a robotics context, which is verified by our concurrent work (Schenck and Fox, 2017), in which we apply our methodology to a robot control task.

The rest of this paper is laid out as follows. The next section details relevant work related to ours. The following section details the exact tasks we investigate in this paper. The section after that describes how we generate our simulated dataset. The next section details how we collect the pouring trials on our robot, followed by a discussion of our learning methodology. We then describe how we evaluate our networks and present experimental

results. And finally the last section concludes the paper and summarizes the results.

## Related Work

Humans interact with liquids from a young age. Studies have shown that even infants can distinguish between rigid objects and “substances” or liquids (Hespos and VanMarle, 2012). They have also shown that infants as young as five months have knowledge about how substances behave and interact with solid objects (Hespos et al., 2016). Furthermore, infants as young as 10 months have the ability to distinguish quantities of non-cohesive substances as greater or less than, although the quantity ratio must be larger for substances than for solid objects, suggesting that humans use a different mechanism to quantify substances than to quantify objects (VanMarle and Wynn, 2011). Further studies have shown a correlation between humans’ understanding of fluid dynamics and what would be expected of a probabilistic fluid physics model (Bates et al., 2015), which suggests that humans have more than a simple perceptual understanding of fluid physics.

However, there has been little work in robotics on creating deep understandings of liquids. Much of the work in robotics involving liquids focuses on the task of pouring (Langsfeld et al., 2014; Okada et al., 2006; Tamosiunaite et al., 2011; Cakmak and Thomaz, 2012). All of these works, though, constrain the task space enough so as to preclude the need for any direct perception of or detailed reasoning about liquids. For example in (Cakmak and Thomaz, 2012) the focus was on learning the overall pouring trajectory, so the robot simply upended the source over the target without needing to know the specifics of the liquid dynamics, only that the source could only be inverted over the target. Work by Rozo *et al.* (Rozo et al., 2013) did have the robot pour a specific amount of liquid into the target, which is more challenging than simply dumping all the contents from the source, however they used their robot’s precise proprioceptive sensors to measure the liquid amount, bypassing the need for any sort of liquid understanding. Many robots do not have precise

proprioceptive sensors, making relying on them for liquid perception infeasible.

There has been some prior work in robotics focusing on physics-based understanding of liquids. Work by Kunze and Beetz (Kunze, 2014; Kunze and Beetz, 2015) utilized a robotic physics simulator to reason about the outcomes of different actions taken by their robot. Specifically, the robot was tasked with finding the best sequence of actions to fry pancakes, which involved reasoning about the liquid pancake batter while pouring and mixing it. However, they simulated the liquid batter as a collection of small balls which had different physics than real pancake batter, and they did not connect the simulated environment to any real-world sensory data. This resulted in a system that, while it worked well in simulation, does not translate well to a real robotic environment.

Similar work by Yamaguchi and Atkeson also utilized a robotic simulator with small balls in place of liquid. In (Yamaguchi and Atkeson, 2015, 2016a), they utilize this simulator to learn fluid dynamics models and perform planning over pouring trajectories. Similar to prior work on robotic pouring, the robot poured all the contents from the source to the target, however in this case they utilized the simulator to reason about spilled liquid. They also applied this framework to a robot in a real environment (Yamaguchi and Atkeson, 2016c), although they used a constant color background and fixed color features to detect the liquid. In more recent work (Yamaguchi and Atkeson, 2016b), they utilized optical flow in addition to a set of heuristics to perceive the liquids in a real-world environment, although the output labels were imprecise and could only detect liquid in the air and not liquid resting in a container. Nonetheless, in this paper we evaluate using optical flow for perception of liquids in combination with deep neural networks.

While (Kunze, 2014; Kunze and Beetz, 2015; Yamaguchi and Atkeson, 2015, 2016a) all used small balls in place of liquid in their simulations, work in computer graphics has developed realistic fluid simulations (Bridson, 2015). Work by Ladický *et al.* (Ladický *et al.*, 2015) used regression forests to learn the particle interactions in the fluid simulation,

resulting in realistic fluid physics, showing that machine learning methods are capable of learning fluid dynamics. Additionally, the work in (Kunze, 2014; Kunze and Beetz, 2015; Yamaguchi and Atkeson, 2015, 2016a) was ungrounded, i.e., it was disconnected from real-world sensory data. Work by Mottaghi *et al.* (Mottaghi *et al.*, 2016b,a) has shown how physical scene models can be connected to real visual data. Specifically, they utilize convolutional neural networks (CNNs) to convert an image into a description of a scene, and then apply Newtonian physics to understand what will happen in future timesteps. In this paper we also utilize CNNs to convert raw sensory data into a labeled scene.

There has been some work in robotics on *perceiving* liquids. Rankin *et al.* (Rankin and Matthies, 2010; Rankin *et al.*, 2011) investigated ways to detect pools of water from an unmanned ground vehicle navigating rough terrain. However, they detected water based on simple color features or sky reflections, and didn't reason about the dynamics of the water, instead treating it as a static obstacle. Griffith *et al.* (Griffith *et al.*, 2012) learned to categorize objects based on their interactions with running water, although the robot did not detect or reason about the water itself, rather it used the water as a means to learn about the objects. In contrast to (Griffith *et al.*, 2012), we use vision to directly detect the liquid itself, and unlike (Rankin and Matthies, 2010; Rankin *et al.*, 2011), we treat the liquid as dynamic and reason about it.

This paper builds on our prior work (Schenck and Fox, 2016, 2017). In (Schenck and Fox, 2016) we utilized CNNs to both detect and track liquids in a realistic fluid simulator. We found that recurrent CNNs are best suited to perceive and reason about liquids. In this paper we show how deep neural networks can be utilized on not only simulated data, but also on data collected on a real robot. We show in work concurrent to this that a robot can use the liquid perception and reasoning capabilities developed in this paper to solve a real robotic task (Schenck and Fox, 2017), specifically learning to pour a specific amount of liquid from only raw visual data.

## Task Overview

In this paper we investigate the dual tasks of *perception* and *reasoning* about liquids. We define *perception* to be determining what in the raw sensory data is liquid, and what is not liquid. We call this task *detection*. We define *reasoning* to be, given labels for the visible liquid (i.e., a working detector), determining where all the liquid is, even if it may not be directly perceivable (e.g., liquid inside a container). We call this task *tracking*. For this paper, we focus on the task of pouring as it requires reasoning about both where the visible liquid is as well as where hidden liquid is.

We evaluate our neural networks on the tasks of *detection* and *tracking* in both simulation and on data collected on a real robot. For the simulated dataset, we generated a large amount of pouring sequences using a realistic liquid simulator. As it is simple to get the ground truth state from the simulator, we can easily evaluate both tasks on the simulated data. For the real-world data, we collected a series of pouring trials on our robot. We use a thermal camera in combination with heated water to acquire the ground truth pixel labels. However, this only gives labels for *visible* liquid, and not liquid occluded by the containers, so we evaluate only the task of *detection* on the robot data.

## Simulated Data Set

We use the simulated dataset generated in our prior work (Schenck and Fox, 2016) to evaluate our methodology. The dataset contains 10,122 pouring sequences that are 15 seconds long each, for a total of 4,554,900 images. Each sequence was generated using the 3D-modeling program Blender (Blender Online Community, 2016) and the library El'Beem for liquid simulation, which is based on the lattice-Boltzmann method for efficient, physically accurate liquid simulations (Körner et al., 2006).

We divide the data generation into two steps: liquid simulation and rendering. Liquid simulation involves computing the trajectory of the mesh of the liquid over the course of the pour. Rendering is converting the state of the simulation at each point

in time into color images. Liquid simulation is much more computationally intensive than rendering\*, so by splitting the data generation process into these two steps, we can simulate the trajectory of the liquid and then re-render it multiple times with different render settings (e.g., camera pose) to quickly generate a large amount of data. We describe these two steps in the following sections.

### Liquid Simulation

The simulation environment was set up as follows. A 3D model of the target container was placed on a flat plane parallel to the ground, i.e., the “table.” Above the target container and slightly to the side we placed the source container. This setup is shown in Figure 1a. The source container is pre-filled with a specific amount of liquid. The source then rotates about the y-axis following a fixed trajectory such that the lip of the container turns down into the target container. The trajectory of the liquid is computed at each timestep as the source container rotates. Each simulation lasted exactly 15 seconds, or 450 frames at 30 frames per second.

For each simulation, we systematically vary 4 variables:

- *Source Container* - cup, bottle, or mug
- *Target Container* - bowl, dog dish, or fruit bowl
- *Fill Amount* - 30%, 60%, or 90%
- *Trajectory* - partial, hold, or dump

The 3 source containers we used are shown in Figures 2a, 2b, and 2c, and the 3 target containers we used are shown in Figures 2d, 2e, and 2f. Each source container was filled either 30%, 60%, or 90% full at the start of each simulation. The source was rotated along one of three trajectories: It was rotated until it was slightly past parallel with the table, held for 2 seconds, then rotated back to upright (partial); It was rotated until it was slightly past parallel with the table, where it stayed for the remainder of the simulation (hold); or It was rotated quickly until it was pointing nearly

---

\*Generating one 15 second sequence takes about 7.5 hours to simulate the liquid and an additional 0.5 hours to render it on our Intel Core i7 CPUs.

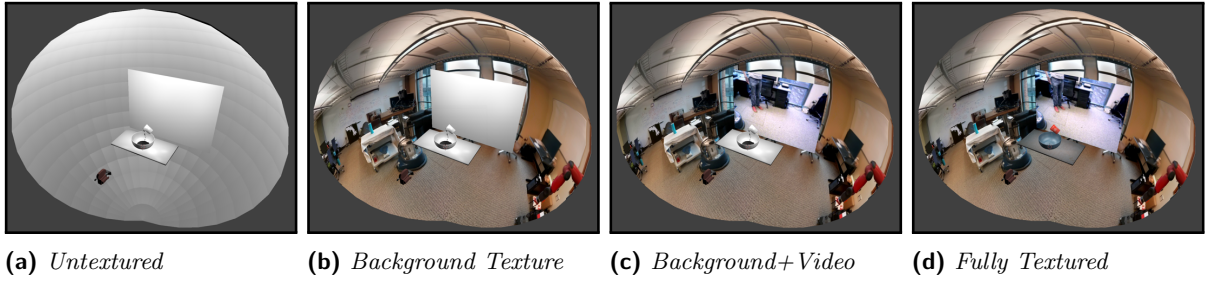


**Figure 1.** The scene used to simulate pouring liquids. The background sphere is cut-away to show its interior. From left to right: The scene shown without any texture or materials; The background image sphere texture added; The video on the plane added in addition to the background texture; and The scene fully textured with all materials.

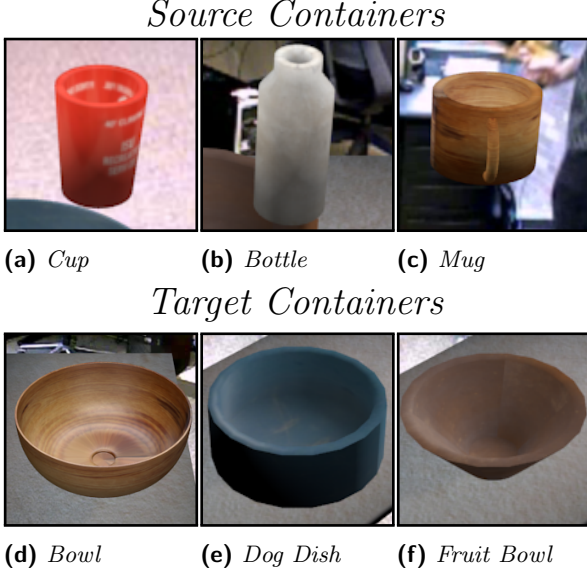


**Figure 2.** The objects used to generate the simulated dataset. The first row are the three source containers. The last row are the 3 target containers. The objects are each shown here with 1 of their possible 7 textures.

vertically down into the target container, remaining there until the simulation finished (dump). The result was 81 liquid simulations (3 sources  $\times$  3 targets  $\times$  3 fill amounts  $\times$  3 trajectories).

## Rendering

To generate rendered pouring sequences, we randomly select a simulation and render parameters<sup>†</sup>. We place the camera in the scene so that it is pointing directly at the table top where the target and source containers are. In order to approximate realistic reflections on the liquid's surface, we enclose the scene in a sphere with a photo sphere taken in our lab set as the texture (shown in Figure 1b). Next we place a video of activity in our lab behind the table opposite the camera (shown in Figure 1c). We took videos such that they approximately match the location in the image on the background sphere behind the video plane. We randomly select a texture for the source and target containers, and we render the liquid as 100% transparent (but including reflections and refractions). Figure 1d shows the full scene with textures, video, and background sphere.

We randomly select from the following N parameters for each rendered sequence:

- *Source Texture* - 7 preset textures
- *Target Texture* - 7 preset textures
- *Activity Video* - 8 videos
- *Camera Azimuth* - 8 azimuths
- *Camera Height* - high or low
- *Camera Distance* - close, medium, or far

---

<sup>†</sup>The number of parameters makes it infeasible to evaluate every possible combination.

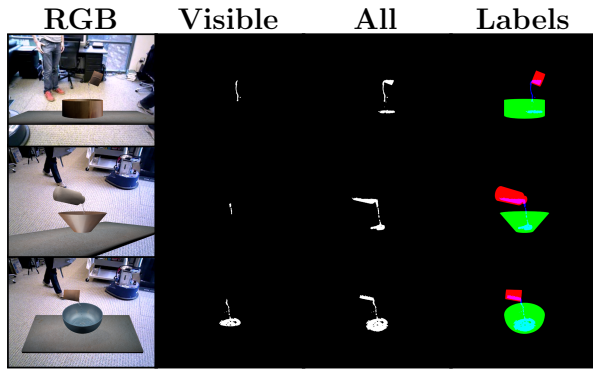


**Figure 3.** Examples of frames from the simulated dataset. The left column is the raw RGB images generated by the renderer; the center-left column shows the ground truth liquid location for visible liquid; the center-right column shows the ground truth liquid location for all liquid in the scene; the right column shows the ground truth labeling output by the simulator.

There are 48 total camera viewpoints. The camera azimuth is randomly selected from 1 of 8 possibilities spaced evenly around the table. The height of the camera is selected such that it is either looking down into the target container at a 45 degree angle (high, lower-left image in Figure 3) or it is level with the table looking directly at the side of the target (low, upper-left image in Figure 3). The camera is also placed either close to the table, far from the table, or in between. The output of the rendering process is a series of color images, one for each frame of the sequence.

### Generating the Ground Truth

We generate the ground truth for each image in each rendered sequence as follows. For each object (source container, target container, and liquid), we set that object to render as a solid color irrespective of lighting (red, green, and blue respectively). Then we make all other objects in the scene invisible, and render the resulting scene. We then combine the images for the objects as separate channels of a single image (right column of Figure 3).

For the tasks of *detection* and *tracking*, we need to be able to distinguish between *visible* and *all* liquid respectively. To do this, we render the scene again



**Figure 4.** The robot used in the experiments in this paper. It is shown here in front of a table, holding the *bottle* in its right gripper, with the *fruit bowl* placed on the table.

with each object rendered as its respective color, and then we encode which object is on top in the alpha channel of the ground truth image described in the last paragraph. Some examples of the result are shown in Figure 3. The left column shows the rendered color image, the right column shows the ground truth pixel labels (absent the alpha channel), and the middle columns show the visible or all liquid.

## Robot Data Set

### Robot

The robot used to collect the data set is shown in Figure 4. It is a Rethink Robotics Baxter Research Robot, an upper-torso humanoid robot with 2 7-dof arms, each with a parallel gripper. The robot is placed in front of a table with a towel laid over it to absorb spilled water. The robot is controlled via joint velocity commands. In the experiments in this paper, the robot uses only one of its arms at a time. The arm is fixed above the target container and the robot controls the joint velocity of its last joint, i.e., the rotational angle of its wrist.

## Sensors

The robot is equipped with a pair of cameras mounted to its front immediately below its screen. The first camera is an Asus Xtion RGBD camera, capable of providing both color and depth images at  $640 \times 380$  resolution and 30 Hz. The second camera is an Infrared Cameras Inc. 8640P Thermographic camera, capable of providing thermal images at  $640 \times 512$  resolution and 30 Hz. The thermal camera is mounted immediately above the RGBD camera's color sensor, and is angled such that the two cameras view the same scene from largely similar perspectives. The Baxter robot is also equipped with joint-torque sensors, however the signal from these sensors is too unreliable and so we did not use them in the experiments in this paper.

**Calibration of the Thermal Camera** For our experiments, we use the thermal camera in combination with heated water to acquire the ground truth pixels labels for the liquid. To do this, we must calibrate the thermal and RGBD cameras to each other. In order to calibrate the cameras, we must know the correspondence between pixels in each image. To get this correspondence, we use a checkerboard pattern printed on poster paper attached to an aluminum sheet. We then mount a bright light to the robot's torso and shine that light on the checkerboard pattern while ensuring it is visible in both cameras. The bright light is absorbed at differing rates by the light and dark squares of the pattern, resulting in a checkerboard pattern that is visible in the thermal camera<sup>‡</sup>.

We then use OpenCV's `findChessboardCorners` function to find the corners of the pattern in each image, resulting in a set of correspondence points  $P^{therm}$  and  $P^{RGB}$ . We compute the affine transform  $T$  between the two sets using singular-value decomposition. Thus to find the corresponding pixel from the thermal image to the RGB image,

simply multiply as follows

$$Tp^{therm} = p^{RGB}$$

where  $p^{therm}$  is the  $xy$  coordinates of a pixel in the thermal image, and  $p^{RGB}$  are its corresponding  $xy$  coordinates in the RGB image.

It should be noted that  $T$  is only an affine transformation in pixel space, not a full registration between the two images. That is,  $T$  is only valid for pixels at the specific depth for which it was calibrated, and for pixels at different depths,  $Tp^{therm}$  will not correspond to the same object in the RGB image as  $p^{therm}$  in the thermal image. While methods do exist to compute a full registration between RGB and thermal images (Pinggera et al., 2012), they tend to be noisy and unreliable. For our purposes, since the liquids are always a constant depth from the camera, we opted to use this affine transform instead, which is both faster and more reliable, resulting in better ground truth pixel labels. While our RGBD camera does provide depth values at each pixel, the liquid does not appear in the depth readings and thus we could not use them to compute the full registration. Figure 5 shows an example of the correspondence between the thermal image and the RGB image.

## Objects

For the robot dataset, we used two sets of objects: *source containers* and *target containers*. We used 3 different source containers, the *cup*, the *bottle*, and the *mug*, shown in 6a, 6b, and 6c. The *bottle* and *mug* were both thermally insulated, and we wrapped the *cup* in insulators. This was done so that the robot could use the same source container from trial to trial without the object building heat and appearing the same temperature as the liquid in the thermal image. The only exception to this was the lid of the *mug*, which was not thermally insulated. It was submersed in cold water between each trial to prevent heat build-up.

We used two different types of target containers, 3 small containers and 3 large. The 3 small containers were the *small bowl*, the *tan mug*, and the *redgray mug* shown in Figures 6d, 6e, and 6f. The 3 large containers were the *bowl*, the *fruit bowl* and the *pan*

---

<sup>‡</sup>Albeit inverted as the black squares absorb more light than the white, thus appearing brighter in the thermal image. However we only care about the corners of the pattern, which are the same.

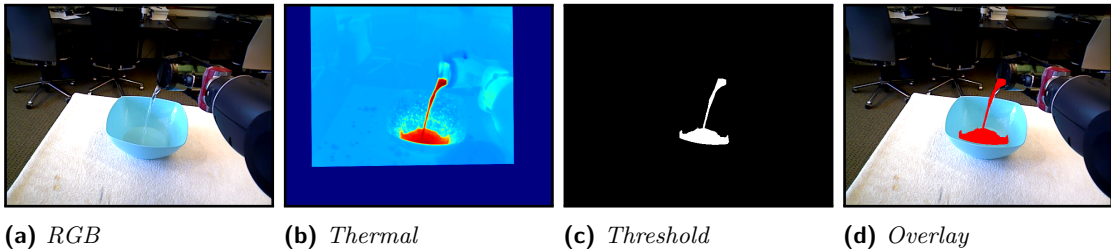


**Figure 5.** An example of obtaining the ground truth liquid labels from the thermal camera. From left to right: The color image from the RGBD camera; The thermal image from the thermal camera transformed to the color pixel space; The result after thresholding the values in the thermal image; and An overlay of the liquid pixels onto the color image.



**Figure 6.** The objects used to collect the dataset for this paper. The first row are the three source containers. The last two rows are the 6 target containers.

shown in 6g, 6h, and 6i. Each target container was

swapped out at the end of each trial to allow it time to dissipate the heat from the hot liquid.

#### Data Collection

We collected 1,009 pouring trials with our robot, generated by combining the data collected in our prior work (Schenck and Fox, 2017) with additional data collected for this paper. For every trial on our robot we collected color, depth, and thermal images. Additionally we collected 20 pouring trials for evaluating our methodology's generalization ability with objects not present in the training set.

We collected 648 pouring trails on our robot for use in this paper. We fixed the robot's gripper over the target container and placed the source container in the gripper pre-filled with a specific amount of liquid. The robot controlled the angle of the source by rotating its wrist joint. We systematically varied 6 variables:

- Arm - left or right
- Source Container - cup, bottle, or mug
- Target Container - bowl, fruit bowl, or pan
- Fill Amount - empty, 30%, 60%, or 90%
- Trajectory - partial, hold, or dump
- Motion - minimal, moderate, or high

We used both arms, as well as varied the source containers. We also used the 3 large target containers to contrast with the 3 small ones used in the prior dataset (described next). In addition to various fill percents, we also included trials with no liquid to provide negative examples. The robot followed three

fixed pouring trajectories: one in which it tilted the source to parallel with the ground and then returned to vertical; one in which it tilted the source to parallel with the ground and held it there; and one in which the robot quickly rotated the source to pointing almost vertically down into the target. Finally, we added motion to the data. For minimal motion, the only motion in the scene was the robot’s with minimal background motion. For moderate motion, a person moved around in the background of the scene while the robot was pouring. For high motion, a person grasped and held the target container and actively moved it around while the robot poured into it.

**Prior Robot Data Collection** In our prior work (Schenck and Fox, 2017) we collected 361 pouring trials. We use that data as part of our dataset for this paper and briefly describe the data collection process here (refer to our prior work for more details).

The robot’s gripper was fixed over the target container and it rotated only its wrist joint. The source container was fixed in the robot’s gripper and pre-filled with a specific amount of liquid. The robot used its controller to attempt to pour a specific amount of liquid, resulting in trajectories where the robot would tilt the source container until some amount of liquid had transferred to the target and then the robot would tilt the source back upright. We used only the *mug* as the source container for these trials and only the *small bowl*, *tan mug*, and *redgray mug* as target containers. The robot used only its right arm. We varied the target amount between 100 and 300 ml and the initial amount of liquid in the source between 300 and 400 ml.

**Test Data** We also collected 20 pouring trials on our robot to evaluate our methodology’s generalization ability on. We used the target containers in Figure 7 which were not included in the training datasets described in the previous sections. For each object, we recorded 3 trials using the *mug* as the source container, the robot’s right arm, and we filled the source initially 90% full. We collected one trial for each of the pouring trajectories described previously (partial, hold, and dump) with minimal background motion. We collected 2 more trials with each object where we fixed the pouring trajectory (fixed as dump)

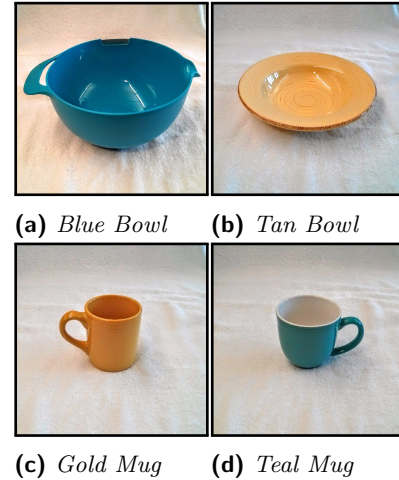


**Figure 7.** The target containers used to create the testing set.

and varied the motion between moderate and high. Overall there were 5 trials per test object for a total of 20 test trials.

### Generating the Ground Truth from Thermal Images

We process the thermal images into ground truth pixel labels as follows. First, we normalize the temperature values for each frame in the range 0 to 1. For all frames before liquid appears, we use the normalization parameters from the first frame with liquid. We then threshold each frame at 0.6, that is, all pixels with values lower than 0.6 are labeled *not-liquid* and all pixels higher are labeled *liquid*.

While this results in a decent segmentation of the liquid, we can further improve it by removing erroneously labeled liquid pixels. For example, during some sequences the robot briefly missed the target container, causing water to fall onto the table and be absorbed by the towel. While this is still technically liquid, we do not wish to label it as such because after being absorbed by the towel, its appearance qualitatively changes. We use the PointCloud Library’s plane fitting and point clustering functions to localize the object on the table from the depth image, and we remove points

belonging to the table<sup>§</sup>. Additionally, for some trials, the lid on the *mug* did not properly cool down between trials, and so for those trials we use a simple depth filter to remove pixels too close to the camera (the source container is slightly closer to the camera than the target).

## Learning Methodology

We utilize deep neural networks to learn the tasks of *detection* and *tracking*. Specifically, we use fully-convolutional networks (FCNs) (Long et al., 2015), that is, networks comprised of only convolutional layers (in addition to pooling and non-linear layers) and no fully-connected layers. FCNs are well suited to the tasks in this paper because they produce pixel-wise labels and because they allow for variable sized inputs and outputs. The following sections describe the different types of inputs and outputs for our networks, as well as the different network layouts.

### Network Input

We implemented 6 different types of input images to feed into our networks. The first was the standard RGB image shown Figure 8a. This is the type of FCN input most commonly seen in the literature (Havaei et al., 2015; Romera-Paredes and Torr, 2015), and we use it as the primary type of input for all *detection* tasks on the simulated dataset. However, since the robot dataset is one tenth the size of the simulated dataset and thus is more prone to overfitting, we also desired to evaluate other types of images that may help counteract this tendency to overfit. The most obvious type of image is grayscale, which was very commonly used in computer vision methods prior to CNNs (Forsyth and Ponce, 2002). Figure 8b shows a grayscale version of the RGB image in Figure 8a.

Inspired by prior work (Yamaguchi and Atkeson, 2016b), we also evaluated optical flow as an input to the networks. We computed the dense optical

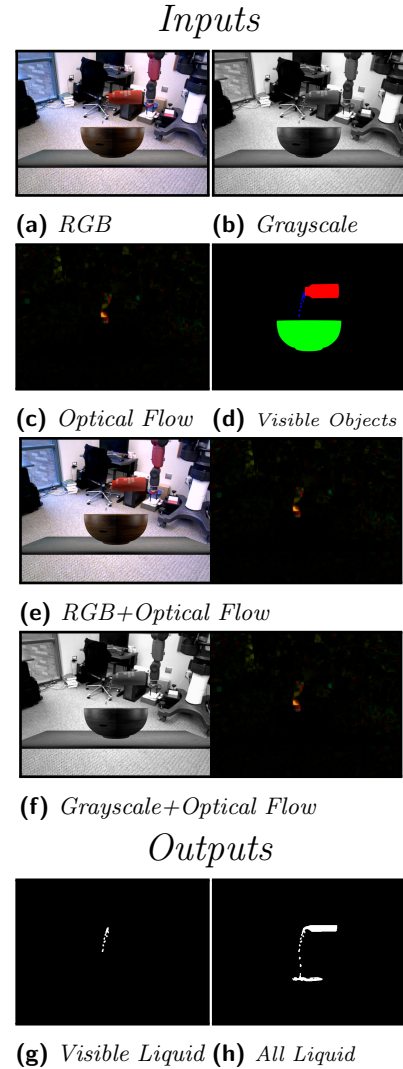


**Figure 8.** Different images of the same frame from the same sequence. The upper part of this figure shows the different types of network inputs (RGB, grayscale, optical flow, visible objects, RGB+optical flow, and grayscale+optical flow). The lower part shows the types of desired network outputs (visible liquid and all liquid).

flow<sup>¶</sup> for a given frame by calling OpenCV's

<sup>§</sup>We keep points above the lip of the target container in the image so as to not remove the stream of liquid as it transfers from the source to the target.

<sup>¶</sup>We also tried sparse optical flow, but the results were much worse.

`calcOpticalFlowFarneback` on that frame and the frame immediately prior (for the first frame we used the following frame instead). For the parameters to the function `calcOpticalFlowFarneback`, we set the number of pyramid levels to 3 and the pyramid scale to 0.5, the window size to 15 and the number of iterations to 3, and the pixel neighborhood size to 5 with a standard deviation of 1.2. Besides calling `calcOpticalFlowFarneback`, we did not perform any other filtering or smoothing on the optical flow output.

The output of the dense optical flow was an xy vector for each pixel, where the vector was the movement of that feature from the first frame to the second. We converted each vector to polar coordinates (angle and magnitude), and further converted the angle to the sine and cosine values for the angle, resulting in three values for each pixel. We store the resulting vectors in a three channel image, where the first channel is the sine of each pixel's angle, the second is the cosine, and the third is the magnitude. An example is shown in Figure 8c (converted to HSV for visualization purposes, where the angle is the hue and the magnitude is the value). While (Yamaguchi and Atkeson, 2016b) showed that optical flow at least correlates with moving liquid, it is not clear that flow by itself provides enough context to solve the *detection* problem. Thus we also evaluate combining it with RGB (Figure 8e) and grayscale (Figure 8f).

For the task of *tracking* we used segmented images as input, that is, if we have a working detector, can the network use the labels from the detector to reason about where all the liquid in an image is? Each input pixel is labeled with the object that is visible at the pixel, which is represented as a one-hot vector (i.e., a binary vector where the index for the corresponding object label is 1 and all the other indices are 0). An example of this is shown in Figure 8d. When visualized, the labels for the source container become the red channel, for the target container become the green channel, and for the liquid become the blue channel. Note that unlike the right column of Figure 3, here the network only gets labels for the object that is “on top” at each pixel and cannot see objects

occluded by other objects, e.g., cannot see the liquid in either container.

### Network Output

The desired output of the network is fixed based on the task. For *detection* the network should output the locations of the *visible* liquid in the scene. An example of this is shown in Figure 8g. Note that in the case of Figure 8g, most of the liquid is occluded by the containers, so here the robot is detecting primarily the flow of liquid as it transfers from the source to the target container.

For *tracking*, the desired output is the location of *all* liquid in the scene, including liquid occluded by the containers. Here the network must learn to infer where liquid is in the scene based on other clues, such as determine the level of liquid in the source container based on the stream of liquid that is visible coming from the opening. An example of this is shown in Figure 8h. We should note that for our two datasets, it is only possible to get the ground truth location of all liquid from the simulated dataset because the simulator allows us to directly see the state of the environment, whereas on the robot dataset, the thermal camera only allows us to see the visible liquid and not liquid occluded by the containers.

The output of each network is a pixel-wise label confidence image, i.e., for each pixel, the network outputs its confidence in [0, 1] that that pixel is either *liquid* or *not-liquid*.

### Network Layouts

All of the networks we use in this paper are fully-convolutional networks (FCNs). That is, they do not have any fully-connected layers, which means each intermediate piece of data in the network maintains the image structure from the original input. This makes FCNs well-suited for tasks which require pixel labels of the pixels from the input image, which both our tasks *detection* and *tracking* require. Additionally, they allow variable sized input and outputs, which we take advantage of during training of our networks (described later in the evaluation section).

We use the Caffe deep learning framework Jia et al. (2014) to implement our networks

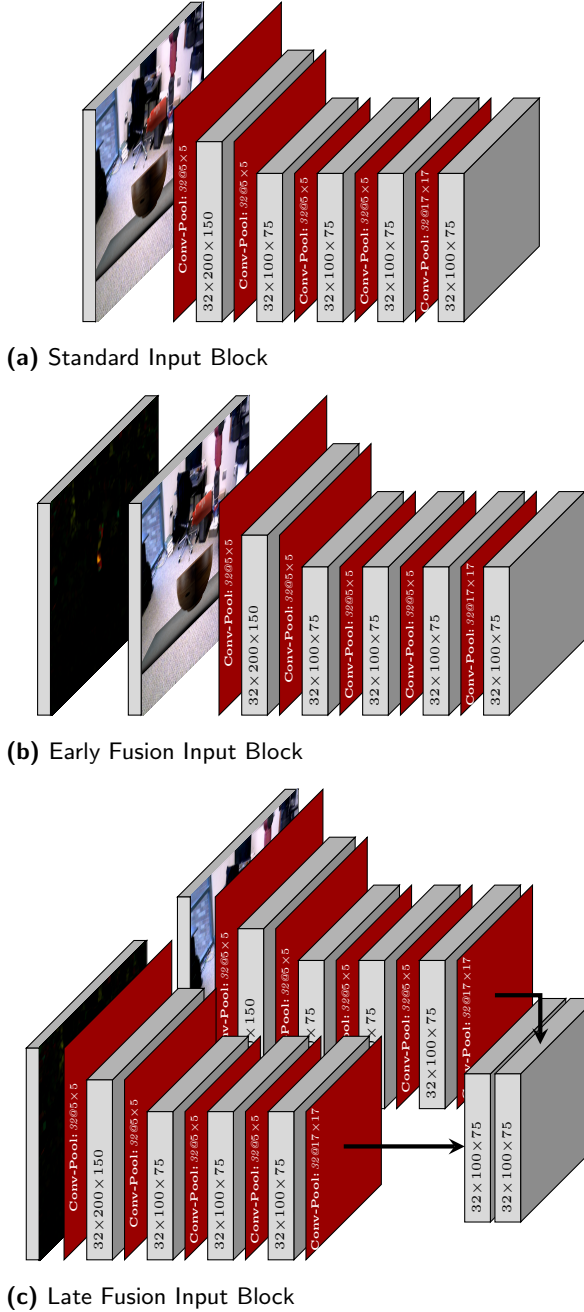
**Input Blocks** Each network we implement is built from one or more input blocks. Input blocks are combinations of network layers with different types of input. Essentially each is the beginning part of an FCN. We split our description of our neural networks into input blocks and network types (below) to simplify it. We combine our different types of input blocks with our different network types to create a combinatorially larger number of networks, which we then used to solve the tasks of *detection* and *tracking*.

Figure 9 shows the 3 different types of input blocks that we use in this paper. The first (Figure 9a) is the standard input block used by most of our networks. It takes as input a single image, which it then passes through 5 conv-pool layers, which apply a convolution, then a rectified linear filter, and finally a max pooling operation. The first two conv-pool layers have a stride of two for the max pooling operation; all other layers have a stride of one. The output of this input block is a tensor with shape  $32 \times \frac{H}{4} \times \frac{W}{4}$  where  $H$  and  $W$  are the height and width of the input image respectively.

The second two input blocks are used for networks that take two different types of images as input (e.g., RGB and optical flow). Figure 9b shows the early-fusion approach, which combines the two images channel-wise and feeds them into a block otherwise identical to the standard input block. Figure 9c shows the late-fusion approach, which feeds each image into separate copies of the standard input block, and then concatenates the resulting tensors channel-wise, resulting in a  $64 \times \frac{H}{4} \times \frac{W}{4}$  tensor. Some work in the literature has suggested that the late-fusion approach tends to perform better than the early-fusion approach (Valada et al., 2016), however in this paper we evaluate this premise on our own tasks.

**Network Types** We use 3 different types of networks in this paper:

**FCN** The first is a standard FCN shown in Figure 10a. It takes the output of the input block and passes it through 2  $1 \times 1$  convolutional layers and a final deconvolutional layer. The  $1 \times 1$



**Figure 9.** The 3 different types of input blocks. The first is used when the network takes only a single type of input; the second two are used when combining two different types of input.

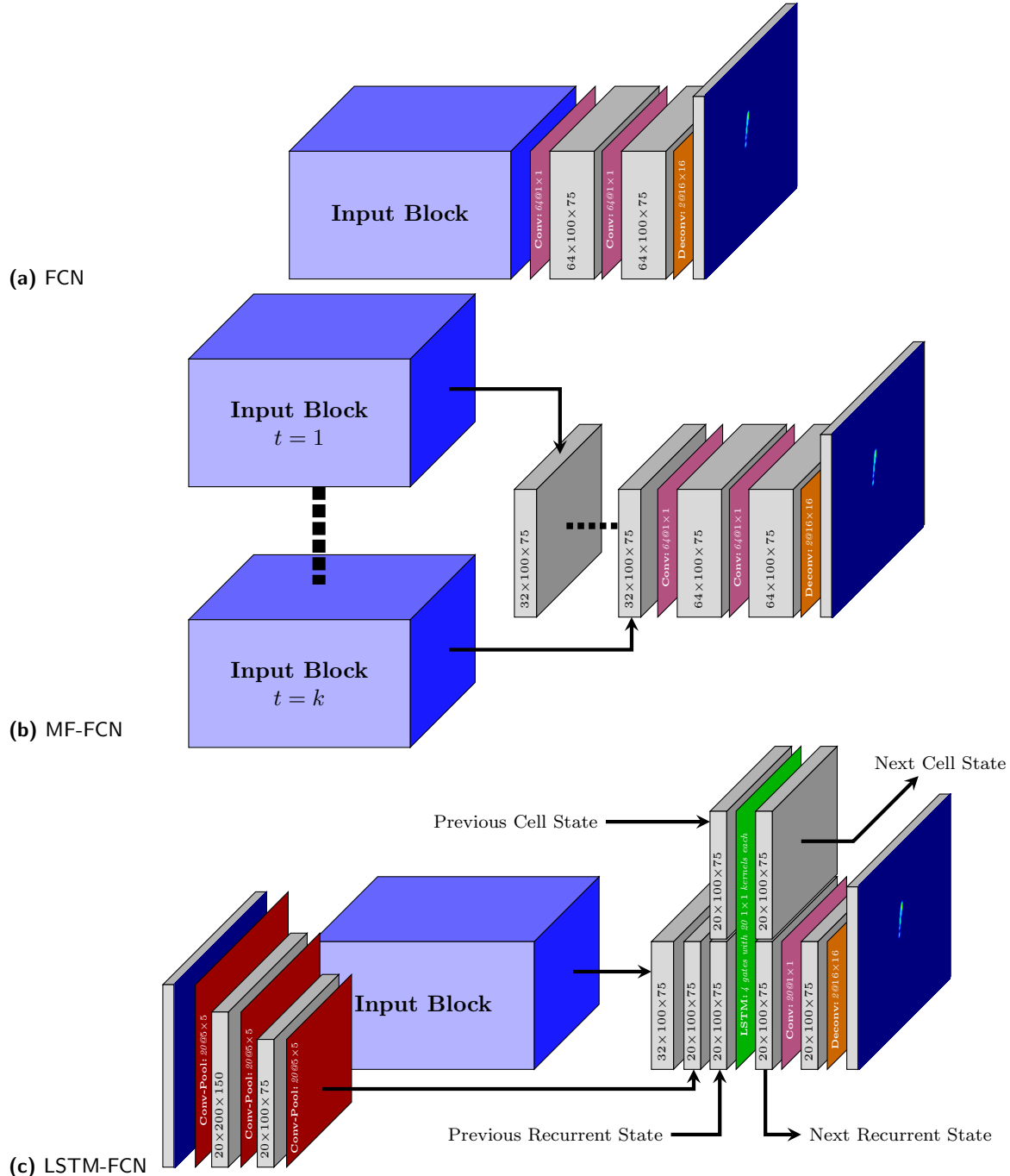


**Figure 10.** The three types of networks we tested. The first is a standard FCN. The second is an FCN that takes in a series of consecutive frames. The final is a recurrent network that uses an LSTM layer to enable the recurrence.

convolutional layers take the place of fully-connected layers in a standard neural network. They take only the channels for a single “pixel” of the input tensor, acting similar to a fully-connected layer on a network that takes the image patch of the response region for that pixel. Each  $1 \times 1$  convolutional layer is followed by a rectified linear filter.

**MF-FCN** The second network type is a multi-frame FCN shown in Figure 10b. It takes as input a series of sequential frames, and so has an input block for each frame. Each input block shares parameters, e.g., the first convolutional layer in the first input block has the exact same kernels as the first convolutional layer in the second input block, and so on. The output tensors of all the input blocks are concatenated together channel-wise. This is then feed to a network structured identical to the structure for the previous network (two  $1 \times 1$  convolutional layers followed by a deconvolutional layer).

**LSTM-FCN** The last network type is a recurrent network that utilizes a long short-term memory (LSTM) layer (Hochreiter and Schmidhuber, 1997) shown in Figure 10c. It takes the recurrent state, the cell state, and the output image from the previous timestep in addition to the frame from the current timestep as input. The output tensor from the input block is concatenated channel-wise with the recurrent state, and with the output image from the previous timestep after it has been passed through 3 conv-pool layers. The resulting tensor is then feed into the LSTM layer along with the cell state. The LSTM layer outputs the cell state for the next timestep as well as the recurrent state for the next timestep. This recurrent state is feed through a  $1 \times 1$  convolutional layer and then a deconvolutional layer to generate the output image for this timestep. To maintain the fully-convolutional nature of our network, we replace all the gates in the LSTM layer with  $1 \times 1$  convolutional layers. Please refer to Figure 1 of (Greff et al., 2015) for a more detailed description of the LSTM layer.

## Evaluation

### Simulated Data Set

We evaluate all three of our network types on the tasks of *detection* and *tracking* on the simulated dataset. For this dataset, we use only single input image types, so all networks are implemented with the standard input block (Figure 9a). We report the results as precision and recall curves, that is, for every value between 0 and 1, we threshold the confidence of the network’s labels and compute the corresponding precision and recall based on the pixel-wise accuracy. We also report the area-under-curve score for the precision and recall curves. Additionally, we report precision and recall curves for various amounts of “slack,” i.e., we count a positive classification as correct if it is within  $n$  pixels of a true positive pixel, where  $n$  is the slack value. This slack evaluation allows us to differentiate networks that are able to detect or track the liquid, albeit somewhat imprecisely, versus networks that fire on parts of the image not close to liquid.

We evaluate our networks on two subsets of the simulated dataset: the *fixed-view* set and the *multi-view* set. The *fixed-view* set contains all the data for which the camera was directly across from the table (camera azimuth of 0 or 180 degrees) and the camera was level with the table (low camera height). Due to the cylindrical shape of all the source and target containers, this is the set of data for which the mapping from the full 3D state of the simulator to a 2D representation is straightforward, which is useful for our networks as they operate only on 2D images. The *multi-view* set contains all data from the simulated dataset, including all camera viewpoints. The mapping from 3D to 2D for this set is not as straightforward.

**Detection** For the task of *detection*, we trained all three networks in a similar manner. Due to the fact that the vast majority of pixels in any sequence are *not-liquid* pixels, we found that trying to train directly on the full pouring sequences resulted in networks that settled in a local minima classifying all pixels as *not-liquid*. Instead, we first pre-train each network for 61,000 iterations on crops of the images

and sequences around areas with large amounts of liquid (due to the increased complexity of the LSTM-FCN, we initialize the pre-training LSTM-FCN with the weights of the pre-trained single-frame FCN). We then train the networks for an additional 61,000 iterations on full images and sequences. This is only possible because our networks are fully-convolutional, which allows them to have variable sized inputs and outputs. Additionally, we also employ gradient weighting to counteract the large imbalance between positive and negative pixels. We multiply the gradient from each *not-liquid* pixel by 0.1 so that the error from the *liquid* pixels has a larger effect on the learned weights.

The full input images to our networks were scaled to  $400 \times 300$ . The crops taken from these images were  $160 \times 160$ . The single-frame networks were trained with a batch size of 32. The multi-frame networks were given a window of 32 frames as input and were trained with a batch size of 1. The LSTM networks were unrolled for 32 frames during training (i.e., the gradients were propagated back 32 timesteps) and were trained with a batch size of 5. We used the mini-batch gradient descent method Adam (Kingma and Ba, 2014) with a learning rate of 0.0001 and default momentum values. All error signals were computed using the softmax with loss layer built-into Caffe (Jia et al., 2014).

**Tracking** For the task of *tracking*, we trained the networks on segmented object labels (Figure 8d). That is, assuming we already have good detectors for what is visible in the scene, can the robot find the liquid that is not visible? Since the input image is already somewhat structured, we scale it down to  $130 \times 100$ . Unlike for *detection*, here we don't pre-train the networks on crops, but we do utilize the same gradient weighting scheme. We use the same training parameters as for *detection* with the exception that we unroll the LSTM network for 160 timesteps. For *tracking*, we use only the *fixed-view* set.

**Combined Detection & Tracking** Finally, we also evaluate performing combined *detection & tracking* with a single network. The networks take in the same  $400 \times 300$  images that the *detection* networks take, and output the location of *all* liquid in the

scene. We initialize these networks with the weights of their corresponding *detection* network and train them on full images. We use the same gradient weighting scheme as for the two tasks separately. We train the networks for combined *detection & tracking* using the same learning parameters as for training the *detection* networks.

### Robot Data Set

For the robot dataset, we evaluate our networks on only the task of *detection* because our thermal camera can only see *visible* liquid and not liquid occluded by the containers. However, *detection* on the robot dataset is more challenging than on the simulated dataset as there is less data to train on. This is a general problem in robotics with deep learning. Deep neural networks require vast amounts of data to train on, but it is difficult to collect this much data on a robot. While there have been some proposed solutions for specific problems (Levine et al., 2015; Tzeng et al., 2015), there is no generally accepted methodology for solving this issue. Here we evaluate utilizing different types of input images to help prevent the networks from overfitting on the smaller amount of data.

Specifically, we train networks for each of the following input types (with the corresponding input block in parentheses):

- RGB (standard input block)
- Grayscale (standard input block)
- Optical Flow (standard input block)
- RGB+Optical Flow (early-fusion input block)
- Grayscale+Optical Flow (early-fusion input block)
- RGB+Optical Flow (late-fusion input block)
- Grayscale+Optical Flow (late-fusion input block)

We train LSTM networks on all of these different types of inputs, as well as the single-frame networks since they are necessary to initialize the weights of the LSTM networks. We used the same learning parameters and training methodology as for *detection* on simulated data (pre-training on crops, gradient weighting, etc.). For brevity, we report our results as area under the curve for the precision and recall curves for each network.

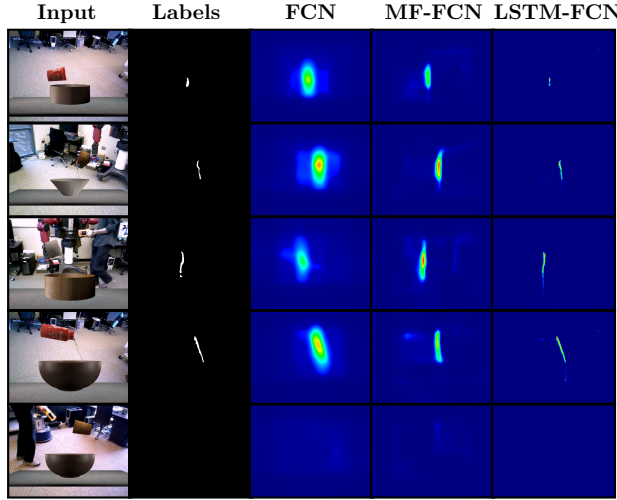


**Figure 11.** Example frames from the 3 network types on the *detection* task on the simulated dataset. The sequences shown here were randomly selected from the test set and the frame with the largest amount of liquid visible was selected. The last sequence was selected to show how the networks perform when no liquid is present.

Unlike for the simulated dataset, where the train and test sets are created by dividing the dataset, for the robot dataset, we created an explicit test set. To test the robot’s generalization ability, we used target containers that did not appear in the train set. We train all networks on the entire dataset and test on this explicit test set. To gauge the extent to which our networks overfit to their training set, we report the performance of the networks on both the train set and the test set.

## Results

### Simulated Data Set

*Detection* Figures 11 and 12 show the results of training our networks for the *detection* task on the simulated dataset. Figure 11 shows the output of each network on example frames. From this figure it is clear that all networks have the ability to at least detect the presence of liquid. However, it is also clear that the MF-FCN is superior to the single-frame FCN, and the LSTM-FCN is superior to the MF-FCN. This aligns with our expectations: As we

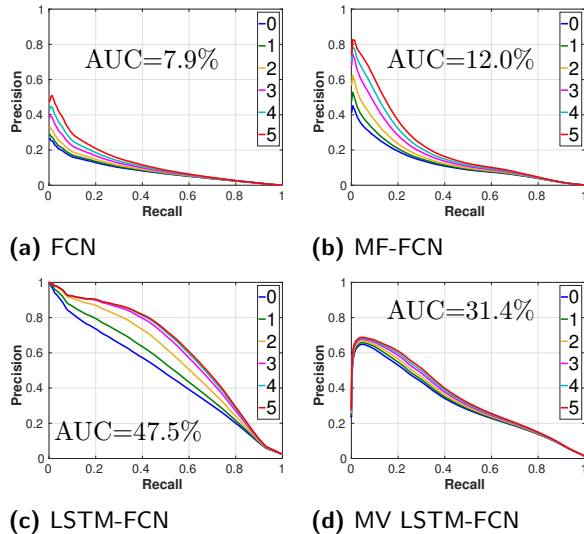


**Figure 12.** Precision-recall curves for *detection* on the simulated dataset. The first three show the curves for the three network types on the *fixed-view* subset. The last graph shows the performance of the LSTM network on the *multi-view* subset. The different lines show the different amounts of slack, i.e., how far a positive classification can be from a true positive to still count as correct. The area under the curve (AUC) is shown for the 0 slack curve.

integrate more temporal information (the FCN sees no temporal information, the MF-FCN sees a small window, and the LSTM-FCN has a full recurrent state), the networks perform better. The quantitative results in Figure 12 confirm these qualitative results.

Since the LSTM-FCN outperformed the other two network types by a significant margin, we evaluated it on the *multi-view* set from the simulated dataset. The performance is shown in Figure 12d. Even with the large increase in camera viewpoints, the network is still able to detect liquid with only a relatively small loss in performance. These results combined with the performance of the LSTM-FCN in Figure 12c clearly show that it is the best network for performing detection and is the reason we focus on this network for detection on the robot dataset.

*Tracking* Figure 13 shows the performance of the 3 network types on the *tracking* task. As expected, the

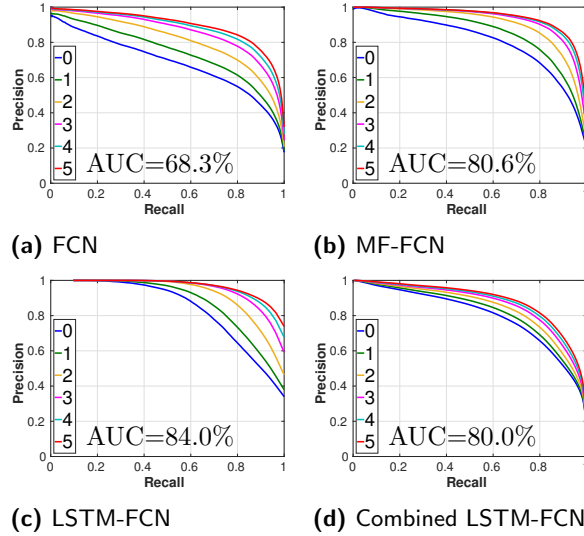


**Figure 13.** The precision-recall curves for the *tracking* task on the simulated dataset. The first 3 show the performance of the three network types on the *tracking* task alone. The last graph shows the performance of the LSTM-FCN on the combined *detection & tracking* task. Similar to Figure 12, the different lines show the different amounts of slack, i.e., how far a positive classification can be from a true positive to still count as correct. The area under the curve (AUC) is shown for the 0 slack curve.

only network with an explicit memory, the LSTM-FCN, performs the best. However, the other two networks perform better than would be expected of networks with no memory capability. This is due to the fact that, given segmented input, the networks can infer where some of the liquid *likely* is. Although it is clear that LSTM-FCNs are best suited for this task.

We additionally tested the LSTM-FCN on the combined *detection & tracking* task. The results are shown in Figure 13d. The network in this case is able to do quite well, with only a minor drop in performance as compared to the LSTM-FCN on the *tracking* task alone.

### Robot Data Set

Figure 15 shows example output on the test set of the LSTM-FCN with different types of input. From this

	Optical Flow		
<small>train test</small>	None	Early-Fusion	Late-Fusion
<b>RGB</b>	<small>76.1% 18.2%</small>	<small>63.3% 17.5%</small>	<small>48.8% 25.1%</small>
<b>Gray</b>	<small>70.7% 22.0%</small>	<small>57.0% 30.5%</small>	<small>73.8% 24.1%</small>
<b>Neither</b>			<small>41.3% 35.1%</small>

	Optical Flow		
<small>train test</small>	None	Early-Fusion	Late-Fusion
<b>RGB</b>	<small>95.1% 23.7%</small>	<small>48.3% 13.4%</small>	<small>93.1% 33.1%</small>
<b>Gray</b>	<small>82.9% 17.9%</small>	<small>81.5% 49.4%</small>	<small>92.8% 41.7%</small>
<b>Neither</b>			<small>82.7% 37.4%</small>

**(a) FCN**

**Figure 14.** The area under the curve (AUC) for the precision-recall curves for the networks for the *detection* task on the robot dataset. The top table shows the AUC for the single-frame FCN; the bottom shows the AUC for the LSTM-FCN. The tables show the AUC for different types of input, with rows for different types of image data (RGB or grayscale) and the columns for different types of optical flow (none, early-fusion, or late-fusion). Each cell shows the AUC on the train set (upper) and the AUC on the test set (lower).

figure, it appears that the best performing network is the one that takes as input grayscale images plus optical flow with the early-fusion input block. Indeed, the numbers in the table in Figure 14b confirm this. Interestingly, the grayscale + optical flow early-fusion network is the second worst performing network on the train set, but performs the best on the test set. This suggests that the other networks tend to overfit more to the training distribution and as a result don't generalize to new data very well.

The table in Figure 14a reflects a similar, albeit slightly different, result for single-frame FCNs. While the grayscale plus optical flow early-fusion network has one of the highest performances on the test set, it is outperformed by the network that takes only optical flow as input. As counter-intuitive as

Color	Labels	RGB	Gray	RGB+Flow Early-Fusion	Gray+Flow Early-Fusion	RGB+Flow Late-Fusion	Gray+Flow Late-Fusion	Flow

**Figure 15.** Example frames for the LSTM-FCN for the *detection* task on the robot dataset with different types of input images. The left column shows the color image for reference and the column immediately to the right of it shows the ground truth. All these images are from the test set with target object not seen in the train set.

it may seem, this makes some sense. The single-frame FCN does not have the ability to view any temporal information, however since optical flow is computed between two frames, it implicitly encodes temporal information in the input to the network. As we saw in the section on detection on the simulated dataset, temporal information is very important for the *detection* task and the network that takes only optical flow is forced to only use temporal information, thus allowing it to generalize to new data better. In the case of the LSTM-FCN, this effect is less pronounced because the network can store temporal information in its recurrent state, although performance of the optical flow only network is still better than performance of the networks that do not use optical flow in any way.

**Initializing on Simulated Data** We also evaluated whether or not the simulated data set, with its larger size, could be used to pre-train the weights of a network that would then be trained on the robot data. Since the LSTM-FCN with grayscale plus optical flow early-fusion as input generalized the best in the previous section, we trained another LSTM-FCN on the same type of input. However, instead of pre-training it on cropped images from the robot dataset, we went through the full training process for a detection network on the simulated dataset,

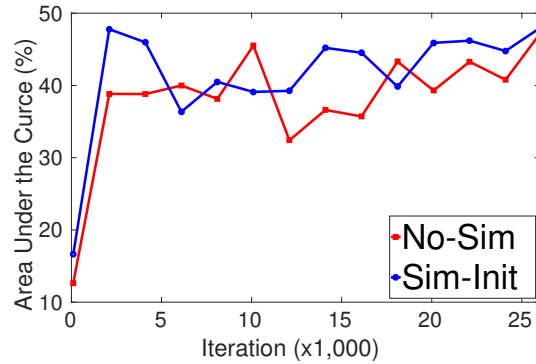


**Figure 16.** The area under the curve on the test set at each iteration of training. The red line shows the performance of the LSTM-FCN trained solely on the robot dataset; the blue line shows the performance of the LSTM-FCN initialized from the simulated dataset.

and used those weights to initialize this network, which was then trained on the robot dataset. The networks converged to the same performance after 61,000 iterations of training. Figure 16 shows the performance of both the network not initialized with any simulated data as compared to the performance

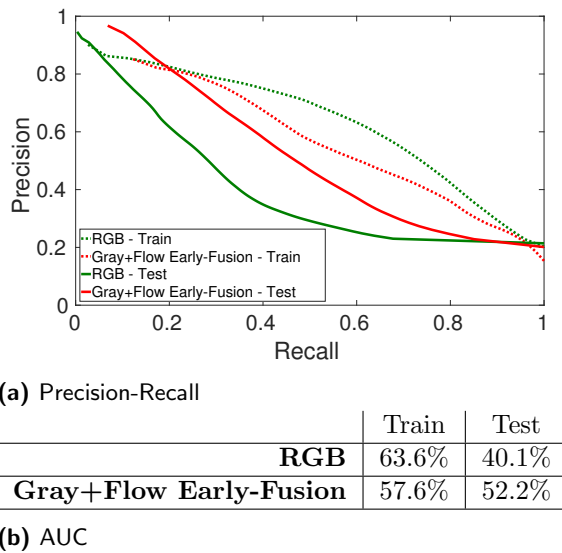


**Figure 17.** The performance on the *tracking* task of the LSTM-FCN that takes as input RGB images compared to the performance of the LSTM-FCN that takes as input grayscale images plus optical flow using the early-fusion input block. The upper graph shows the precision-recall plot for both networks on both the train and test sets. The lower table shows the corresponding area under the curve for each curve.

of this network on the test set at each iteration. The network initialized with simulated data does seem to converge slightly faster, although not by a large amount. Nonetheless, it does appear that the simulated data can be used to initialize the networks and get slightly faster convergence.

### Tracking Revisited

The prior section showed that an LSTM-FCN taking as input grayscale early-fused with optical flow has the ability to generalize better than any other type of network we evaluated. This result was achieved on the *detection* task, and we wanted to see if this translates to the *tracking* task. However, the robot data set does not contain the ground truth for

tracking, so we return to the simulated dataset to test this hypothesis.

We train two networks: one that takes the default input of RGB images and one that takes grayscale images early-fused with optical flow. We train them on the combined *detection & tracking* task. They are trained in the same manner as described previously for doing combined *detection & tracking*. The advantage of using this alternative input type is its ability to generalize to new data, so we hold out all pouring sequences with one of the target containers (the *dog dish*) during training. This includes during training of all pre-trained networks such that the final weights of the networks were never influenced by any data containing the test object.

Figure 17 shows the performance of the two networks on both the train and test sets. From this figure it is clear that the RGB network outperforms the other on the training set, however, the gray+flow early-fusion network outperforms the RGB network on the test set. This confirms the results we found in the previous section: Networks trained with grayscale early-fused with optical flow generalize better to new situations.

### Conclusion

In this paper, we showed how a robot can solve the tasks of *detection* and *tracking* liquids using deep learning. We evaluated 3 different network architectures, FCN, MF-FCN, and LSTM-FCN, all of which integrated different amounts of temporal information. We also evaluated eight different types of input images to our networks, including RGB and grayscale combined with optical flow. We tested these networks on both data we generated in a realistic liquid simulator and on data we collected from a real robot.

Our results clearly show that integrating temporal information is crucial for perceiving and reasoning about liquids. The multi-frame FCN was able to outperform the single-frame FCN because it incorporated a window of frames, giving it more temporal information. Furthermore, the LSTM-FCN was able to outperform the MF-FCN because it has an explicit recurrent state, allowing it to remember

information much longer than the fixed window of the MF-FCN. This was true not only for the task of *tracking*, which requires a notion of memory, but also for the task of *detection*.

The results also showed that, for the purposes of generalizing to new objects and settings, standard RGB images were not as well suited as images converted to grayscale and early-fused with optical flow. Networks trained on RGB images tended to perform very well on sequences drawn from the same distribution as their training set, but their performance dropped considerably when those sequences were drawn from a slightly different setting. However, while networks trained on grayscale early-fused with optical flow did not reach the same level of performance on data taken from the training distribution, their generalization to new settings was significantly better.

This paper also introduced a new dataset, the University of Washington Liquid Pouring Dataset (UW-LPD), which we make available to the wider research community via the following url: <http://rse-lab.cs.washington.edu/1pd/> The total size of all the data collected is approximately 2.5 terabytes.

This paper opens up various avenues for future work. We show in our concurrent work (Schenck and Fox, 2017) that the methods introduced in this paper can be successfully applied to a robotic pouring task. However, in that work, the robot maintains the 2D liquid reasoning from this work. A next step for future work would be to look at ways that enables robots to reason about liquids in full 3D and take advantage of that to do more complex manipulation tasks. Another avenue for future work is to investigate more ways for networks to generalize to new data. In this paper the test data, while different from the training data, was still collected in the same environment with the same setup. Future work will examine methods for training networks to generalize to liquids across many different environments with many different conditions.

## References

- Bates CJ, Yildirim I, Tenenbaum JB and Battaglia PW (2015) Humans predict liquid dynamics using probabilistic simulation. In: *Proceedings of the 37th annual conference of the cognitive science society*.
- Blender Online Community (2016) *Blender - A 3D modelling and rendering package*. Blender Foundation, Blender Institute, Amsterdam. URL <http://www.blender.org>.
- Bridson R (2015) *Fluid simulation for computer graphics*. CRC Press.
- Cakmak M and Thomaz AL (2012) Designing robot learners that ask good questions. In: *ACM/IEEE International Conference on Human-Robot Interaction (HRI)*. pp. 17–24.
- Farabet C, Couprie C, Najman L and LeCun Y (2013) Learning hierarchical features for scene labeling. *Pattern Analysis and Machine Intelligence, IEEE Transactions on* 35(8): 1915–1929.
- Forsyth DA and Ponce J (2002) *Computer vision: a modern approach*. Prentice Hall Professional Technical Reference.
- Girshick R, Shotton J, Kohli P, Criminisi A and Fitzgibbon A (2011) Efficient regression of general-activity human poses from depth images. In: *Computer Vision (ICCV), 2011 IEEE International Conference on*. IEEE, pp. 415–422.
- Greff K, Srivastava RK, Koutnýk J, Steunebrink BR and Schmidhuber J (2015) Lstm: A search space odyssey. *arXiv preprint arXiv:1503.04069* .
- Griffith S, Sukhoy V, Wegter T and Stoytchev A (2012) Object categorization in the sink: Learning behavior-grounded object categories with water. In: *Proceedings of the 2012 ICRA Workshop on Semantic Perception, Mapping and Exploration*. Citeseer.
- Guo X, Singh S, Lee H, Lewis RL and Wang X (2014) Deep learning for real-time atari game play using offline monte-carlo tree search planning. In: *International Conference on Neural Information Processing Systems (NIPS)*. pp. 3338–3346.

- Havaei M, Davy A, Warde-Farley D, Biard A, Courville A, Bengio Y, Pal C, Jodoin PM and Larochelle H (2015) Brain tumor segmentation with deep neural networks. *arXiv preprint arXiv:1505.03540* .
- Hespos SJ, Ferry AL, Anderson EM, Hollenbeck EN and Rips LJ (2016) Five-month-old infants have general knowledge of how nonsolid substances behave and interact. *Psychological science* 27(2): 244–256.
- Hespos SJ and VanMarle K (2012) Physics for infants: Characterizing the origins of knowledge about objects, substances, and number. *Wiley Interdisciplinary Reviews: Cognitive Science* 3(1): 19–27.
- Hochreiter S and Schmidhuber J (1997) Long short-term memory. *Neural computation* 9(8): 1735–1780.
- Jia Y, Shelhamer E, Donahue J, Karayev S, Long J, Girshick R, Guadarrama S and Darrell T (2014) Caffe: Convolutional architecture for fast feature embedding. *arXiv preprint arXiv:1408.5093* .
- Kingma D and Ba J (2014) Adam: A method for stochastic optimization. *arXiv preprint arXiv:1412.6980* .
- Körner C, Pohl T, Rüde U, Thürey N and Zeiser T (2006) Parallel lattice boltzmann methods for cfd applications. In: *Numerical Solution of Partial Differential Equations on Parallel Computers*. Springer, pp. 439–466.
- Krizhevsky A, Sutskever I and Hinton GE (2012) Imagenet classification with deep convolutional neural networks. In: *Advances in neural information processing systems*. pp. 1097–1105.
- Kunze L (2014) *Naïve Physics and Commonsense Reasoning for Everyday Robot Manipulation*. PhD Thesis, Technische Universität München.
- Kunze L and Beetz M (2015) Envisioning the qualitative effects of robot manipulation actions using simulation-based projections. *Artificial Intelligence* .
- Ladický L, Jeong S, Solenthaler B, Pollefeys M and Gross M (2015) Data-driven fluid simulations using regression forests. *ACM Transactions on Graphics (TOG)* 34(6): 199:1–199:9.
- Langsfeld JD, Kaipa KN, Gentili RJ, Reggia JA and Gupta SK (2014) Incorporating failure-to-success transitions in imitation learning for a dynamic pouring task. In: *IEEE International Conference on Intelligent Robots and Systems (IROS) Workshop on Compliant Manipulation*.
- Levine S, Finn C, Darrell T and Abbeel P (2015) End-to-end training of deep visuomotor policies. *arXiv preprint arXiv:1504.00702* .
- Long J, Shelhamer E and Darrell T (2015) Fully convolutional networks for semantic segmentation. In: *IEEE International Conference on Computer Vision and Pattern Recognition (CVPR)*. pp. 3431–3440.
- Mottaghi R, Bagherinezhad H, Rastegari M and Farhadi A (2016a) Newtonian image understanding: Unfolding the dynamics of objects in static images. In: *Proceedings of the Conference of Computer Vision and Pattern Recognition (CVPR)*.
- Mottaghi R, Rastegari M, Gupta A and Farhadi A (2016b) “what happens if...” learning to predict the effect of forces in images. In: *Proceedings of the European Conference on Computer Vision (ECCV)*.
- Okada K, Kojima M, Sagawa Y, Ichino T, Sato K and Inaba M (2006) Vision based behavior verification system of humanoid robot for daily environment tasks. In: *IEEE-RAS International Conference on Humanoid Robotics (Humanoids)*. pp. 7–12.
- Pinggera P, Breckon T and Bischof H (2012) On cross-spectral stereo matching using dense gradient features. In: *IEEE Conference on Computer Vision and Pattern Recognition (CVPR)*.
- Rankin A and Matthies L (2010) Daytime water detection based on color variation. In: *IEEE/RSJ International Conference on Intelligent Robots and Systems (IROS)*. pp. 215–221.

- Rankin AL, Matthies LH and Bellutta P (2011) Daytime water detection based on sky reflections. In: *IEEE International Conference on Robotics and Automation (ICRA)*. pp. 5329–5336.
- Romera-Paredes B and Torr PH (2015) Recurrent instance segmentation. *arXiv preprint arXiv:1511.08250*.
- Rozo L, Jimenez P and Torras C (2013) Force-based robot learning of pouring skills using parametric hidden markov models. In: *IEEE-RAS International Workshop on Robot Motion and Control (RoMoCo)*. pp. 227–232.
- Schenck C and Fox D (2016) Towards learning to perceive and reason about liquids. In: *Proceedings of the International Symposium on Experimental Robotics (ISER)*.
- Schenck C and Fox D (2017) Visual closed-loop control for pouring liquids. In: *Proceedings of the International Conference on Experimental Robotics (ICRA) (under review)*. ArXiv:1610.02610.
- Tamosiunaite M, Nemec B, Ude A and Wörgötter F (2011) Learning to pour with a robot arm combining goal and shape learning for dynamic movement primitives. *Robotics and Autonomous Systems* 59(11): 910–922.
- Tzeng E, Devin C, Hoffman J, Finn C, Peng X, Levine S, Saenko K and Darrell T (2015) Towards adapting deep visuomotor representations from simulated to real environments. *arXiv preprint arXiv:1511.07111*.
- Valada A, Oliveira G, Brox T and Burgard W (2016) Deep multispectral semantic scene understanding of forested environments using multimodal fusion. In: *Proceedings of the International Symposium on Experimental Robotics (ISER)*.
- VanMarle K and Wynn K (2011) Tracking and quantifying objects and non-cohesive substances. *Developmental science* 14(3): 502–515.
- Yamaguchi A and Atkeson C (2016a) Differential dynamic programming for graph-structured dynamical systems: Generalization of pouring behavior with different skills. In: *Proceedings of the International Conference on Humanoid Robotics (Humanoids)*.
- Yamaguchi A and Atkeson C (2016b) Stereo vision of liquid and particle flow for robot pouring. In: *Proceedings of the International Conference on Humanoid Robotics (Humanoids)*.
- Yamaguchi A and Atkeson CG (2015) Differential dynamic programming with temporally decomposed dynamics. In: *IEEE-RAS International Conference on Humanoid Robotics (Humanoids)*. pp. 696–703.
- Yamaguchi A and Atkeson CG (2016c) Neural networks and differential dynamic programming for reinforcement learning problems. In: *IEEE International Conference on Robotics and Automation (ICRA)*. pp. 5434–5441.